Supporting information for

On-surface synthesis of antiaromatic and open-shell indeno[2,1-*b*]fluorene polymers and their lateral fusion into porous ribbons

Marco Di Giovannantonio,[1,*] Kristjan Eimre,[1] Aliaksandr V. Yakutovich,[1] Qiang Chen,[2] Shantanu Mishra,[1] José I. Urgel,[1] Carlo A. Pignedoli,[1] Pascal Ruffieux,[1] Klaus Müllen,[2,3] Akimitsu Narita,[2,4,*] Roman Fasel[1,5,*]

[1]*Empa, Swiss Federal Laboratories for Materials Science and Technology, nanotech@surfaces Laboratory, 8600 Dübendorf, Switzerland*
[2]*Max Planck Institute for Polymer Research, 55128 Mainz, Germany*
[3]*Institute of Physical Chemistry, Johannes Gutenberg University Mainz, Duesbergweg 10-14, 55128 Mainz, Germany*
[4]*Organic and Carbon Nanomaterials Unit, Okinawa Institute of Science and Technology Graduate University, Okinawa 904-0495, Japan*
[5]*Department of Chemistry and Biochemistry, University of Bern, 3012 Bern, Switzerland*

Table of Contents

1. Precursor synthesis and characterization

1-1. General Information

All reactions dealing with air- or moisture- sensitive compounds were carried out under protection of Argon using standard vacuum-line and Schlenk techniques. Unless otherwise noted, all starting materials and other reagents were purchased from commercial sources and used as received without further purification. Thin layer chromatography (TLC) were performed on silica gel coated aluminum plates with F254 indicator and preparative column chromatography were performed on silica gel with grain size of 0.063 – 0.200 mm. The Nuclear Magnetic Resonance (NMR) spectra were recorded on Bruker 300 and 700

MHz spectrometers. The chemical shifts (δ) were expressed in ppm relative to the residual signals of deuterated solvent (Abbreviations: s = singlet, d = doublet, dd = double doublet, t = triplet, m = multiplet; CD_2Cl_2 @ 5.32 ppm ^{1}H NMR, @ 53.84 ppm ^{13}C NMR). Thermogravimetric analysis (TGA) was measured on a Mettler Toledo TGA-851 system with a heating speed of 10 K/min under nitrogen atmosphere. High-resolution mass spectra (HRMS) were recorded by matrix-assisted laser decomposition/ionization (MALDI) using 7,7,8,8-tetracyanoquinodimethane (TCNQ) as matrix on a Bruker Reflex II-TOF spectrometer.

1-2. Experimental details and descriptions

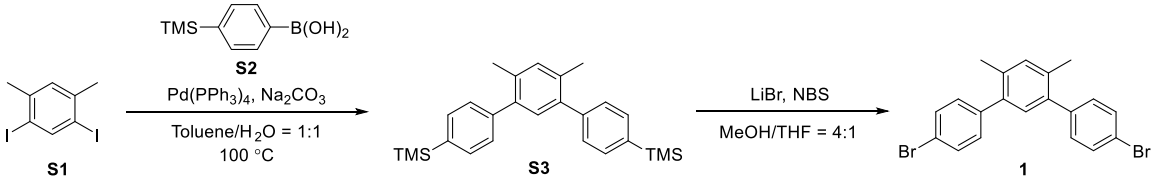

Scheme S1. Synthetic route towards 4,4''-dibromo-4',6'-dimethyl-1,1':3',1''-terphenyl (**1**)

4,4''-bis(trimethylsily)-4',6'-dimethyl-1,1':3',1''-terphenyl (**S3**)

To a 50 mL Schlenk tube equipped with a stirrer bar were added 1,5-diiodo-2,4-dimethylbenzene (**S1**) (1.81 g, 5.06 mmol), 4-(trimethylsilyl)phenylboronic acid (**S2**) (2.61 g, 13.5 mmol) and Na_2CO_3 (3.22 g, 30.4 mmol) under Argon atmosphere. Then, toluene (10 mL) and water (10 mL) were added. After degassing the mixture by three freeze-pump-thaw cycles, $Pd(PPh_3)_4$ (0.600 g, 5.19 mmol) was added. The reaction mixture was heated at 100 °C for 22 h with vigorous stirring until consumption of the starting material was confirmed by TLC (eluent: *n*-hexane). The reaction mixture was then cooled down to a room temperature and extracted twice with ethyl acetate (20 mL). The organic phases were combined, washed with brine (20 mL), dried over Na_2SO_4 and evaporated. The residue was purified by column chromatography (eluent: *n*-hexane:dichloromethane = 50:1) to give the title compound as colorless oil (1.4 g, 69% yield). ^{1}H NMR (300 MHz, Methylene Chloride-d_2) δ 7.58 (d, J = 8.0 Hz, 4H), 7.35 (d, J = 8.0 Hz, 4H), 7.20 (s, 1H), 7.11 (s, 1H), 2.31 (s, 6H), 0.30 (s, 18H); ^{13}C NMR (75 MHz, Methylene Chloride-d_2) δ 142.5, 139.8, 139.0, 134.6, 133.5, 132.9, 131.6, 129.0, 20.2, –1.0; HRMS (MALDI-TOF): *m/z* Calcd for $C_{26}H_{34}Si_2$: 402.2199 $[M]^+$, found: 402.2298.

4,4''-dibromo-4',6'-dimethyl-1,1':3',1''-terphenyl (**1**)

To a solution of 4,4''-bis(trimethylsily)-4',6'-dimethyl-1,1':3',1''-terphenyl (**S3**) (1.4 g, 3.5 mmol) in a mixture of methanol (40 mL) and tetrahydrofuran (20 mL) were added LiBr (786 mg, 9.05 mmol) and *N*-bromosuccinimide (NBS) (1.6 g, 9.0 mmol). Then the reaction mixture was stirred at room temperature overnight. After completion of the reaction was confirmed by TLC (eluent: *n*-hexane:ethyl acetate = 10:1), the solvents were evaporated under a reduced pressure. The residue was dissolved in ethyl acetate (30 mL) and water (20 mL) and the organic layer was separated. The aqueous phase was extracted twice with ethyl acetate. Combined organic layers were washed with brine (20 mL), dried over Na_2SO_4, and evaporated. The residue was purified by column chromatography (elu-

ent: *n*-hexane:ethyl acetate = 20:1) and recrystallized for four times from ethanol to give the title compound (0.131 g, 9% yield) as needle-like crystals. ^{1}H NMR (700 MHz, Methylene Chloride-d_2) δ 7.54 (d, J = 8.4 Hz, 4H), 7.23 (d, J = 8.4 Hz, 4H), 7.19 (s, 1H), 7.05 (s, 1H), 2.26 (s, 6H); ^{13}C NMR (176 MHz, Methylene Chloride-d_2) δ 140.7, 138.5, 134.8, 132.9, 131.4, 131.3, 130.9, 121.1, 20.0; HRMS (MALDI-TOF): *m/z* Calcd for $C_{20}H_{16}Br_2$: 413.9619 $[M]^+$, found: 413.9628.

2. Computational details

The equilibrium geometries of the molecules adsorbed on the Au(111) surface were calculated with the CP2K code[1] implementing DFT within a mixed Gaussian plane waves approach. The surface/adsorbate systems were modeled within the repeated slab scheme with the simulation cell containing 4 atomic layers of Au along the [111] direction. The slab consisted of 224 surface units corresponding to a size of 41.27 x 40.85 Å^2. A layer of hydrogen atoms was added to passivate one side of the slab in order to suppress the Au(111) surface state. 40 Å of vacuum was added in the direction perpendicular to the surface to decouple the system from its periodic images. The electronic states of C and H were expanded with TZV2P Gaussian basis set and the ones of Au with a DZVP basis set. Norm-conserving Goedecker-Teter-Hutter pseudopotentials[2] were used to represent the frozen core electrons of the atoms. The PBE exchange correlation functional[3] was used together with Grimme's DFT-D3 scheme[4] for van der Waals interactions. The equilibrium geometries were obtained by keeping the bottom two layers of the slab fixed to ideal bulk positions and all other atoms were relaxed until forces were lower than 0.005 eV/Å.

STM images were simulated within the Tersoff-Haman approximation[5] based on the Kohn-Sham orbitals of the slab/adsorbate systems. The orbitals were extrapolated to the vacuum region in order to correct the wrong decay of the charge density due to the localized basis set[6].

The ProbeParticle model[7] was used to simulate AFM images. We used a 2-point implementation of the model where two probe particles represent the carbon and oxygen atoms in the CO molecule. The stiffness parameters of the ProbeParticle as well as the Lennard-Jones parameters of the tip were obtained by fitting to DFT calculations for an isolated PTCDA molecule and an isolated pentacene molecule. The charges of the tip atoms were assigned by the restrained electrostatic potential method[8] applied in the case of the pentacene molecule. For the tip sample electrostatic interactions the Hartree potential obtained from the CP2K calculations was used.

Reactions presented in Supplementary Fig. 6 were simulated with the climbing image nudged elastic band (NEB) method with 12 replicas. The initial guess for the NEB trajectory was found with a chain of geometry optimizations, where a distance constraint between two relevant atoms for the considered reaction was gradually changed in steps of 0.1 Å.

Band structures in Supplementary Fig. 4 were calculated with the Quantum Espresso software package using the PBE exchange correlation functional. The plane wave basis with an energy cutoff of 400 Ry for the charge density was used together with PAW pseudopotentials (SSSP[9]) and a Monkhorst k-mesh of 10 x 1 x 1.

The electronic structure of the isolated oligomers of structure **4** were studied with the Gaussian 09 software package[10]. Geometries were optimized at the U(R)B3LYP/6-311G** level of theory. For the natural orbital occupation number analysis and the $NICS_{zz}$ the basis set of 6-311+G** was used together with the LC-UBLYP exchange correlation functional with the range separation parameter μ of 0.33 $bohr^{-1}$ [11]. The magnetic shielding tensor for $NICS_{zz}$[12] was calculated with the gauge invariant atomic orbital (GIAO) method[13].

3. Additional experimental and computational results

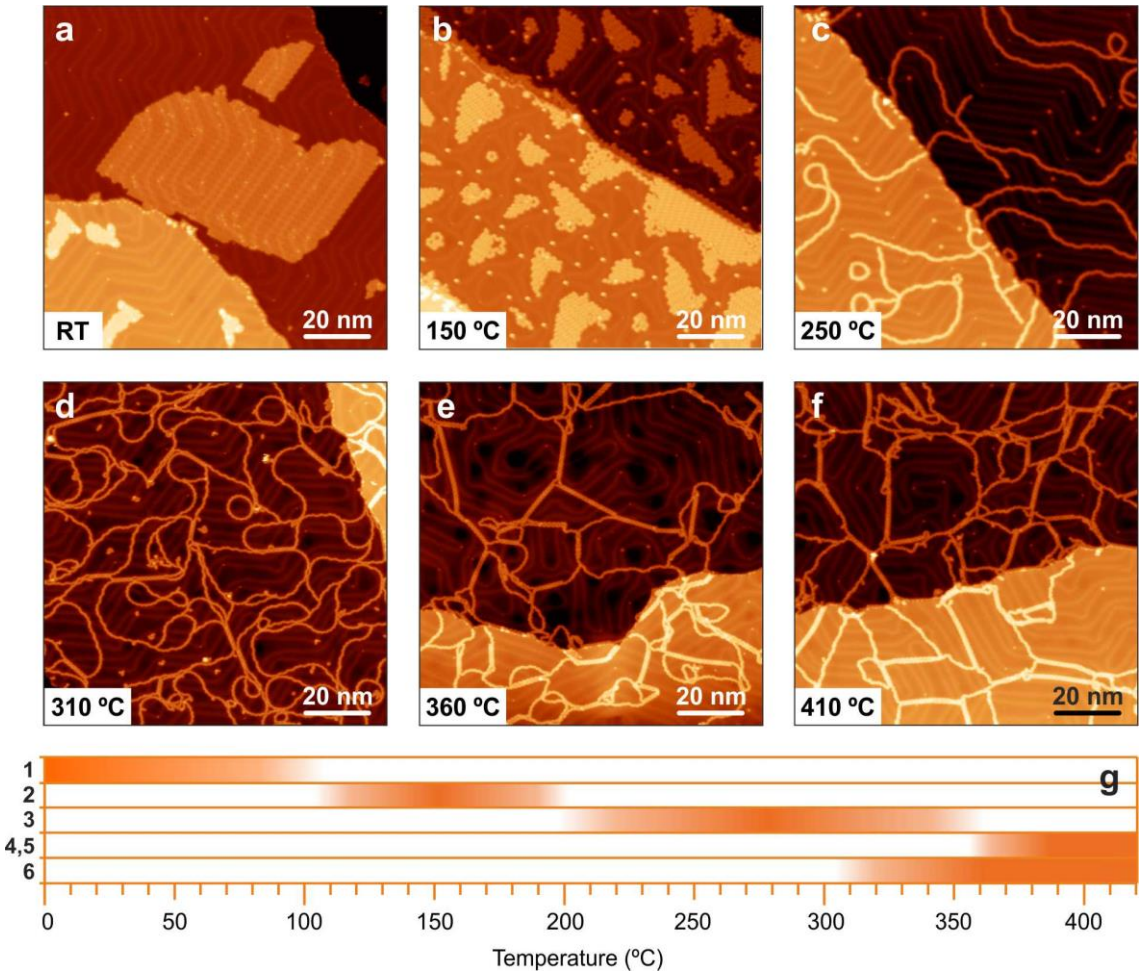

Figure S1. Overview STM images. a-f, Large scale STM images of the Au(111) surface at all the investigated temperatures (indicated for each panel). The sequence of images does not belong to the very same sample, thus the molecular coverage varies from case to case. **g,** Graph illustrating the temperature ranges at which each structure described in the main text is observed, according to the numbering in Fig. 1. The ranges are only indicative, and based on the STM experiments solely. It must be noted that the ribbons **6** are first observed at lower temperature compared to the *poly*-IF **4**. **a**, V_b = –1.5 V, I_t = 10 pA. **b**, V_b = –1.0 V, I_t = 10 pA. **c**, V_b = –1.5 V, I_t = 10 pA. **d**, V_b = –0.3 V, I_t = 50 pA. **e**, V_b = –1.0 V, I_t = 10 pA. **f**, V_b = –1.0 V, I_t = 10 pA.

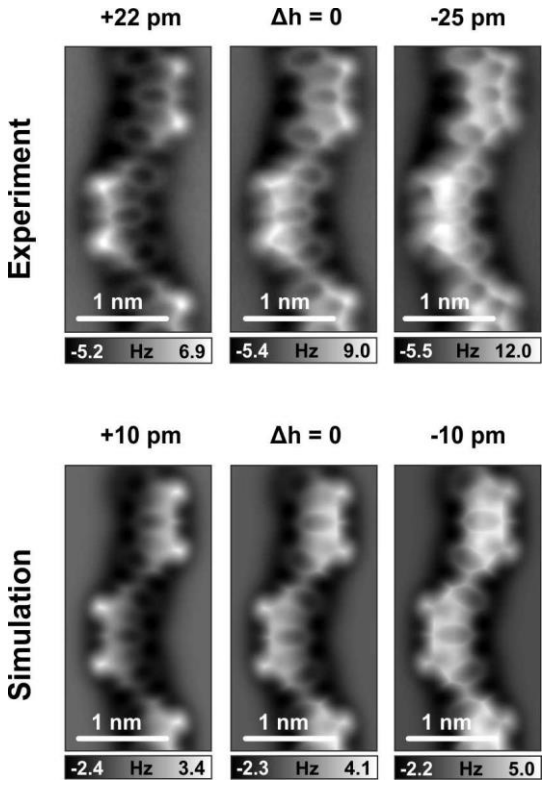

Figure S2. nc-AFM of 3. Height-dependent experimental and simulated nc-AFM images of the polymers observed after annealing the surface at 250 ºC (**3**). In both cases the bright protrusions due to H_2 groups at sp^3 carbons are better visible at larger tip-molecule distances (*i.e.* more positive Δz values). In the experimental nc-AFM image of the center top panel Δz is +2.1 Å with respect to STM set point: –0.005 V, 100 pA.

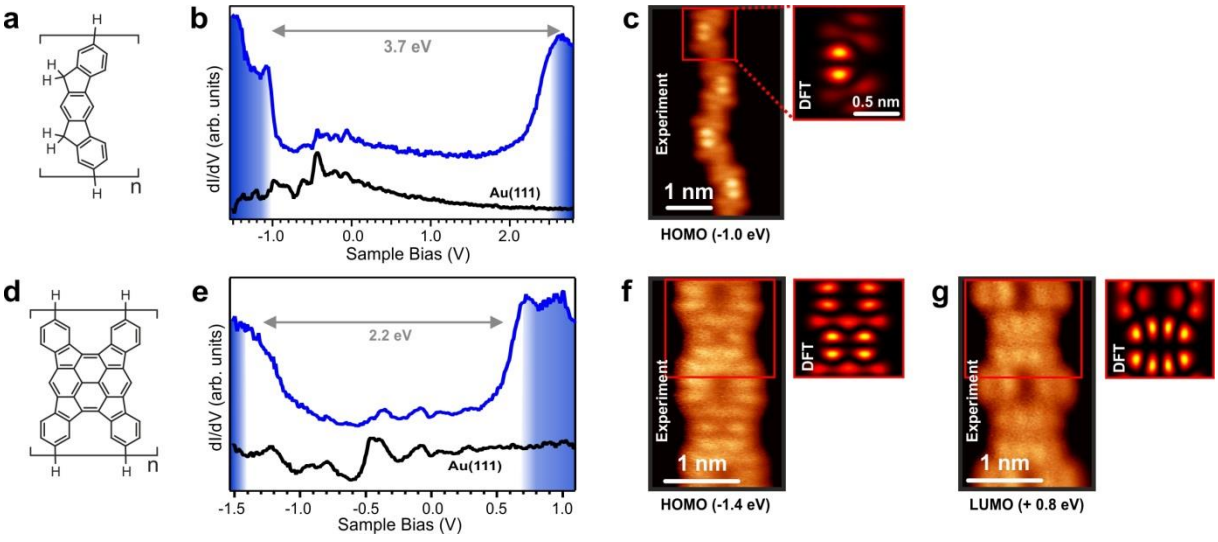

Figure S3. STS of 3 and 6. a,d, Chemical structures investigated. **b,e,** Constant height dI/dV spectra acquired at each structure. **c,f,g,** Constant height dI/dV maps at specific bias voltages (indicated below each image), together with the DFT-calculated LDOS maps of the corresponding structure on unreconstructed Au(111). The good match between experimental and theoretical conductance maps confirms our assignment of the HOMOs and LUMOs. The LUMO of structure **3** could not be mapped since, while scanning at bias voltage of +2.6 V, dehydrogenation of the polymer into the structure **4** occurred, due to a tip-induced process.

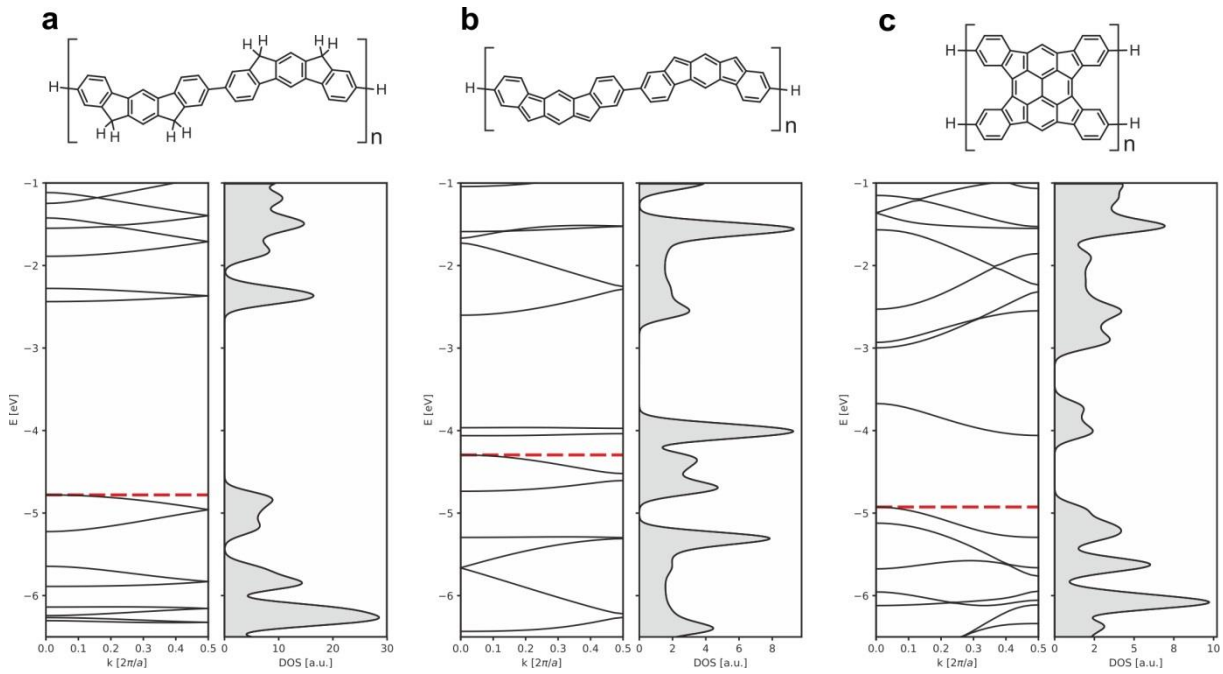

Figure S4. Electronic structure of the isolated periodic polymers 3 and 4, and ribbon 6. a, Band structure and density of states for the polymer corresponding to the chain with doubly hydrogenated carbon atoms at five-membered rings' apexes (structure **3**). The band gap is 2.34 eV. **b,** Band structure and density of states for the polymer corresponding to the chain with singly hydrogenated carbon atoms at five-membered rings' apexes (structure **4**). The band gap is 0.23 eV. This solution corresponds to a spin-singlet solution of the unrestricted DFT calculation, with spin density contributions localized on the five-membered rings (Fig. 5a in the main text). **c,** Band structure and density of states for the ribbons (structure **6**). The band gap is 0.87 eV. The red line represents the maximum of the valence band. The PBE functional was used for all of the mentioned calculations.

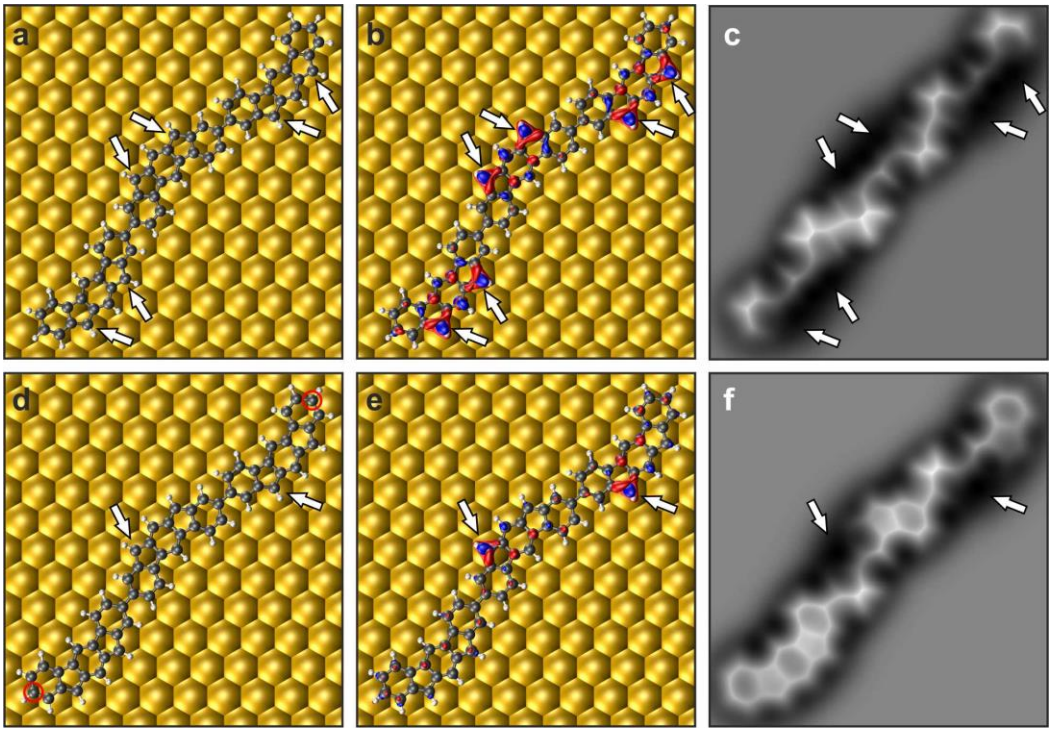

Figure S5. Origin of flat and twisted IF units in *poly*-IF. a, DFT-optimized geometry of an oligomer composed of three IF units on unreconstructed Au(111). All the carbon atoms at five-membered rings' apexes (indicated by the white arrows) lie nearly on top of Au atoms. This induces an interaction between the molecule and the substrate producing locally a considerable change in the charge density of the total system with respect to the sum of charge densities of the isolated molecule and substrate. **b,** Panel **a** with charge density difference isosurfaces at ±0.02 e/Å^3. **c,** nc-AFM simulation of this structure shows a clear lowering of the five-membered rings' apexes, as observed in the experimental images in Fig. 3b,h. This calculation demonstrates that, when a chain is free to relax on the substrate, it will find an optimum position producing the tilt of its units. **d,** The polymers experimentally observed above 310 ºC are always linked to other chains at their ends (see Supplementary Fig. 1d,e), which act as constraints against their complete relaxation on the substrate. Therefore, we simulated this behavior for the same chain as in panel **a**, but starting from the optimized geometry of a trimer of structure **3** (doubly hydrogenated carbon atoms at five-membered rings' apexes, not shown here). After removing the hydrogen atoms to obtain the structure **4** and fixing the x, y positions of the two carbon atoms at the oligomer ends (indicated by the red circles), we calculated the DFT-optimized geometry of this chain. The result is reported in panel **d**. Due to the constraints, only two out of the six carbons at five-membered rings' apexes are now on top of Au atoms (as highlighted by the white arrows), while the others sit close to hollow or bridge positions. **e,** The charge density difference is now localized only at these two carbon atoms, which are the only ones lowered by the interaction with the gold substrate, as evidenced by the nc-AFM simulation in panel **f**. It must be noted that removing the constraints from the geometry in panel **d** leads to the restoring of the geometry in panel **a**.

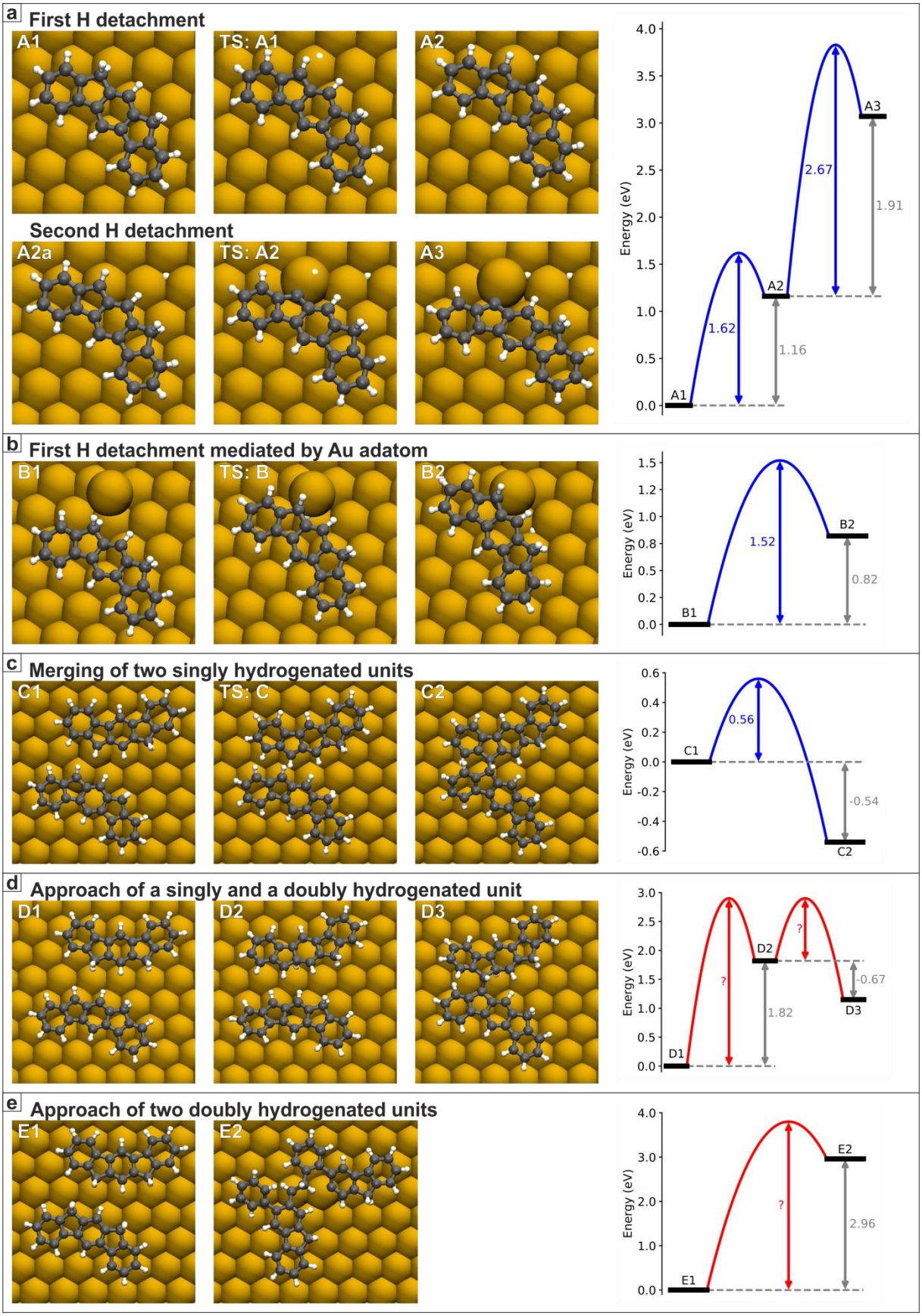

Figure S6. DFT investigation of reactions involving monomers. a, Nudged elastic band (NEB) calculation results for the removal of the first (A1→A2) and second (A2→A3) hydrogen atom from a doubly hydrogenated carbon atom at a five-membered ring's apex. TS: A1 and TS: A2 indicate the corresponding transition states. The energy of A2a is lower than A2 by 0.04 eV due to the detached H being in a different hollow site, which has

been subtracted from the energy values of TS: A2 and A3. **b**, NEB calculation results for the removal of the first hydrogen of a doubly hydrogenated apex carbon atom of a five-membered ring mediated by an Au adatom. **c**, NEB calculation results for the merging of two units at singly hydrogenated carbon atoms at five-membered rings. **d**, Results of a chain of constrained geometry optimizations where a singly hydrogenated apex carbon atom of a five-membered ring of one unit was approached to a doubly hydrogenated apex carbon atom of a five-membered ring of another unit. During the approach, the system reached a stable intermediate D2, where one hydrogen atom of the doubly hydrogenated unit migrated to a neighboring carbon atom. When the C-C bond merging the two units formed, the system ended in a stable state D3. **e**, Results of a chain of constrained geometry optimizations where doubly hydrogenated apex carbon atoms of five-membered rings of two units were approached to each other. The system ended up in a high-energy state E2, where two C-C bonds were broken. In panels **d** and **e**, the NEB calculations to find the barrier heights (labelled by question marks) were not performed, as the energy values of the intermediate D2 or final product E2 already ruled out these reactions.

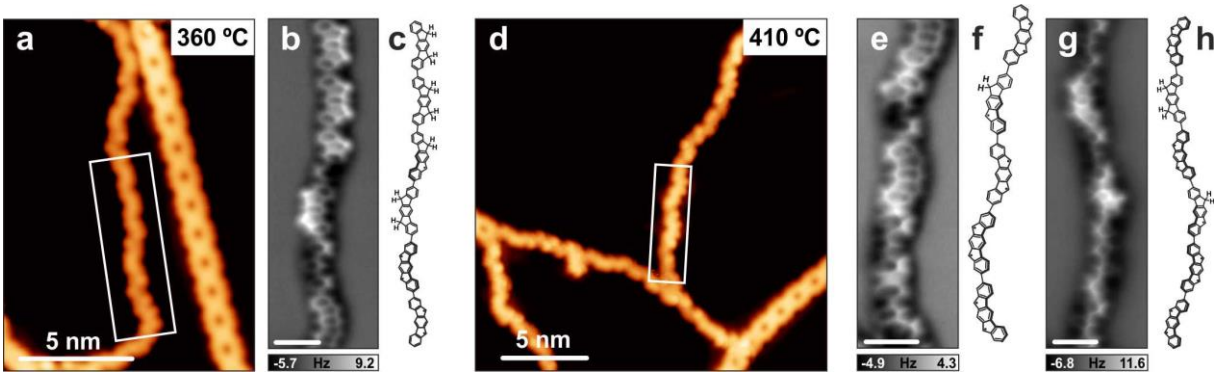

Figure S7. Coexistence of different phases. STM (**a,d**) and nc-AFM (**b,e,g**) images of the surface after annealing to 360 ºC (**a-c**) and 410 ºC (**d-h**), together with the corresponding molecular schemes of the observed structures. These images show that structures **3** and **4** coexists at these temperatures, with progressive reduction of **3** (upon dehydrogenation) with increasing temperature. The nc-AFM images in panels **b** and **e** are acquired at the segments outlined by the white rectangles in panels **a** and **d**, respectively. The image in **g** is acquired at a different position. **a**, V_b = –0.5 V, I_t = 30 pA. **b**, Δz is +2.3 Å with respect to STM set point: –0.005 V, 150 pA. **d**, V_b = –0.3 V, I_t = 50 pA. **e**, Δz is +2.2 Å with respect to STM set point: –0.005 V, 150 pA. **g**, Δz is +2.0 Å with respect to STM set point: –0.005 V, 100 pA. Scale bars in panels **b**, **e**, and **g** are 1 nm.

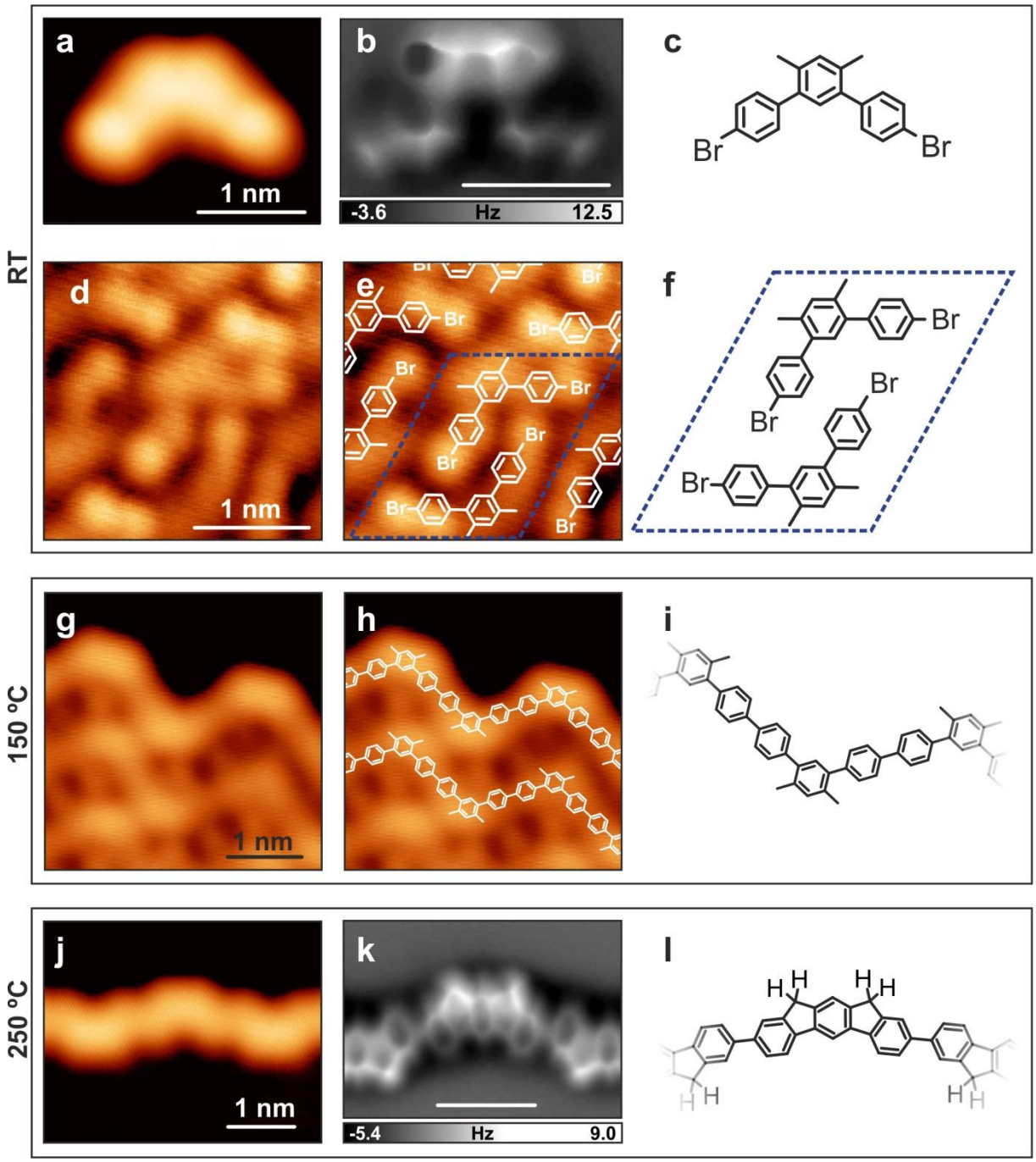

Figure S8. Large magnification of the structures reported in Figure 1 in the main text.

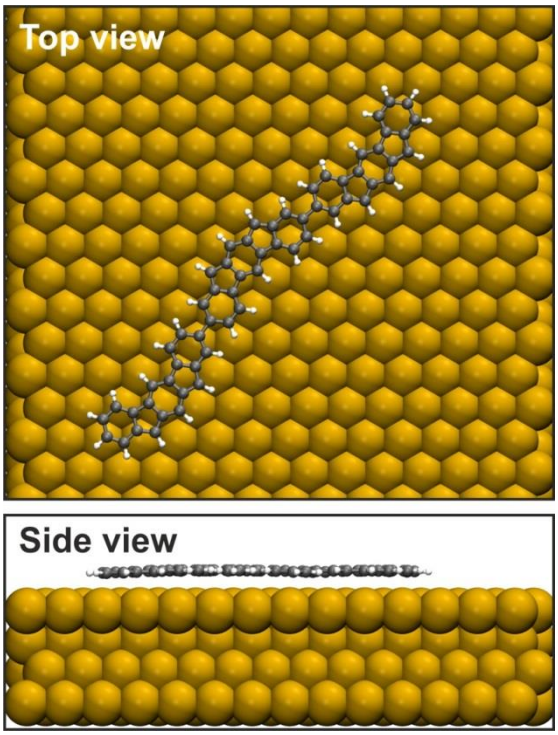

Figure S9. Flat *poly*-IF. DFT-optimized geometry of an oligomer composed of three IF units on unreconstructed Au(111). All the carbon atoms at five-membered rings' apexes lie close to hollow or bridge sites. Therefore, no significant twist of the IF units is observed, their dihedral angle being less than 2 degrees. The sequence of twisted and flat units depends on the initial geometry and is therefore stochastic.

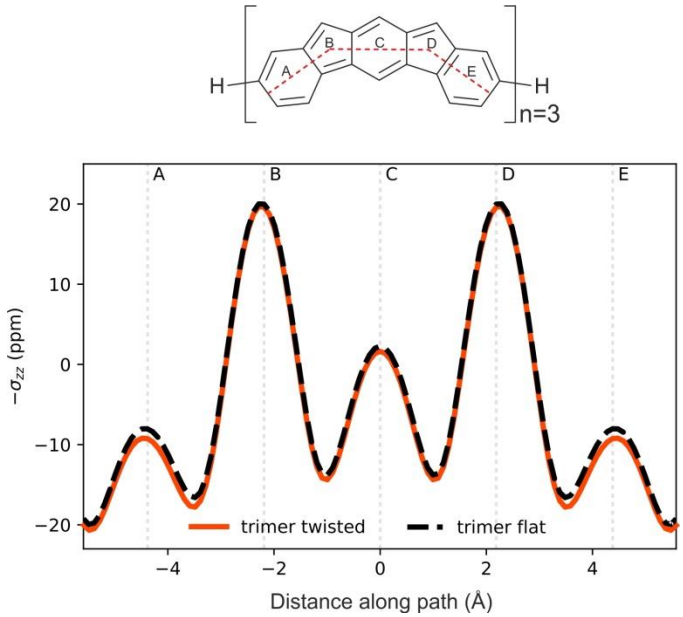

Figure S10. Trimer twisted vs flat. Out-of-plane nucleus-independent chemical shift $NICS_{zz}$-1 (lower panel) calculated at the GIAO-LC-UBLYP/6-311+G** level of theory along the path indicated in the upper panel for the central unit of a trimer (n=3). Two calculations have been performed: (i) the three IF units are coplanar (the dihedral angle between them is zero, trimer flat, black dashed curve), and (ii) the trimer has been relaxed to its equilibrium gas phase geometry, where a dihedral angle of ~35º between the IF units is present (trimer twisted, red solid curve). Clearly, a twist of the IF units does not affect their antiaromaticity. Moreover, the radical character (number of unpaired electrons per monomer, estimated from the occupation numbers with the Head-Gordon expression) is 1.362 and 1.350 for the twisted and flat configuration, respectively. This indicates that also the radical character of *poly*-IF is unchanged upon twist of its constituent IF units.

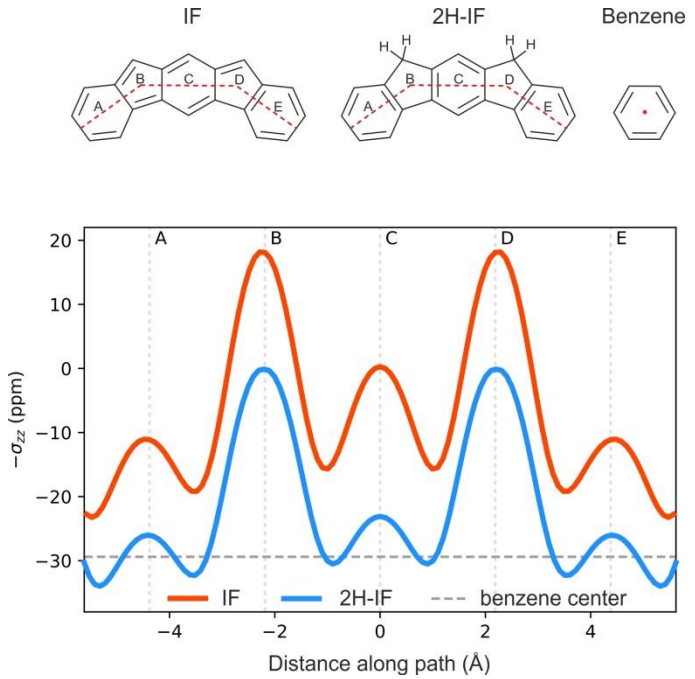

Figure S11. Passivated units. Out-of-plane nucleus-independent chemical shift $NICS_{zz}$-1 (lower panel) calculated at the GIAO-LC-UBLYP/6-311+G** level of theory along the path indicated in the upper panel for isolated IF and 2H-IF units, and compared to the value obtained for benzene. Hydrogenation of the two carbon atoms at the five-membered rings apexes modifies the electronic properties of the unit. The conjugation path does not involve the five-membered rings anymore, which become non-aromatic (sites B and D). The six-membered rings gain aromaticity (sites A, C and E), approaching the value obtained for benzene. Moreover, the computed radical character of 2H-IF is zero. These calculations suggest that the antiaromaticity and radical character of *poly*-IF on Au(111) are maintained only in the flat units, while they might be altered in twisted units, due to their strong interaction with the gold substrate.

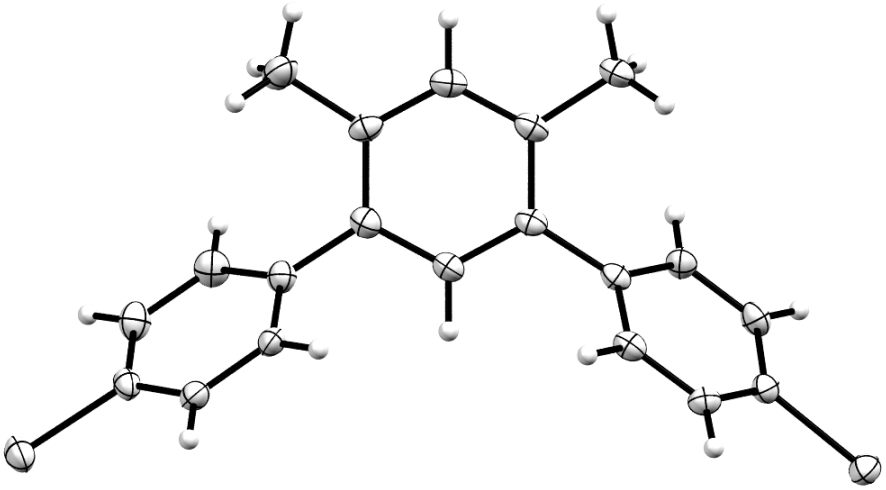

Figure S12. Single crystal structure of monomer 4,4''-dibromo-4',6'-dimethyl-1,1':3',1''-terphenyl (1).

Crystal data for **1** (CCDC 1903872)

formula	$C_{20}H_{16}Br_2$
molecular weight	416.15 $gmol^{-1}$
absorption	μ = 4.830 mm^{-1} corrected with 6 crystal faces
Transmission	T_{min} = 0.242, T_{max} = 0.6464
crystal size	0.1 x 0.11 x 0.64 mm^3 colorless needle
space group	P $2_1/c$ (monoclic)
lattice parameters	a = 13.9524(16)Å
(calculate from	b = 10.5759(8)Å β = 103.738(9)°
10268 reflections with	c = 11.6942(13)Å
2.6° < θ < 28.3°)	V = 1676.2(3)$Å^3$ z = 4 F(000) = 824
temperature	120K
density	d_{xray} = 1.649 gcm^{-3}

Data collection

diffractometer	STOE IPDS 2T
radiation	Mo-K_α Graphitmonochromator
Scan – type	ω scans
Scan – width	1°
scan range	2° ≤ θ < 28°
	-18 ≤ h ≤ 18 -14 ≤ k ≤ 12 -11 ≤ l ≤ 15
number of reflections:	
measured	8039
unique	4053 (R_{int} = 0.4053)
observed	3384 (|F|/σ(F) > 4.0)

Data correction, structure solution and refinement

corrections	Lorentz and polarisation correction.
Structure solution	Program: SIR-2004
refinement	Program: SHELXL-2018 (full matrix). 201 refined parameters, weighting scheme: $w=1/[\sigma^2(F_o^2) + (0.0416*P)^2+4.31*P]$ with $(Max(F_o^2,0)+2*F_c^2)/3$. H-atoms at calculated positions and refined with isotropic displacement parameters, non H- atoms refined anisotropically.
R-values	wR2 = 0.0985 (R1 = 0.0401 for observed reflections, 0.0546 for all reflections)
goodness of fit	S = 1.059
maximum deviation of parameters	0.001 * e.s.d
maximum peak height in diff. Fourier synthesis	0.70, -0.58 $eÅ^{-3}$

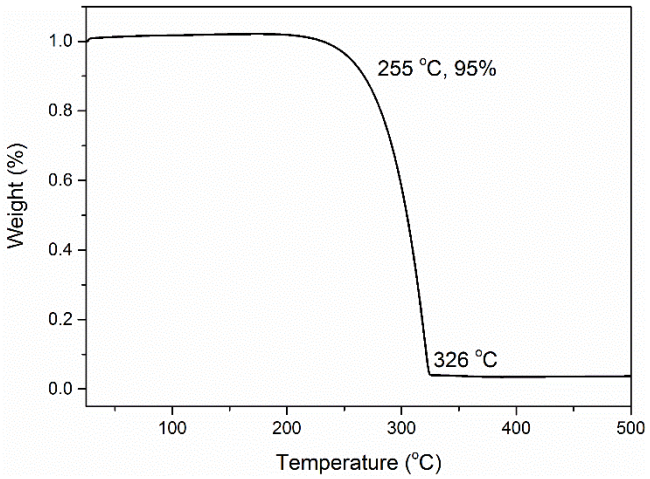

Figure S13. TGA spectra of monomer 4,4''-dibromo-4',6'-dimethyl-1,1':3',1''-terphenyl (1).

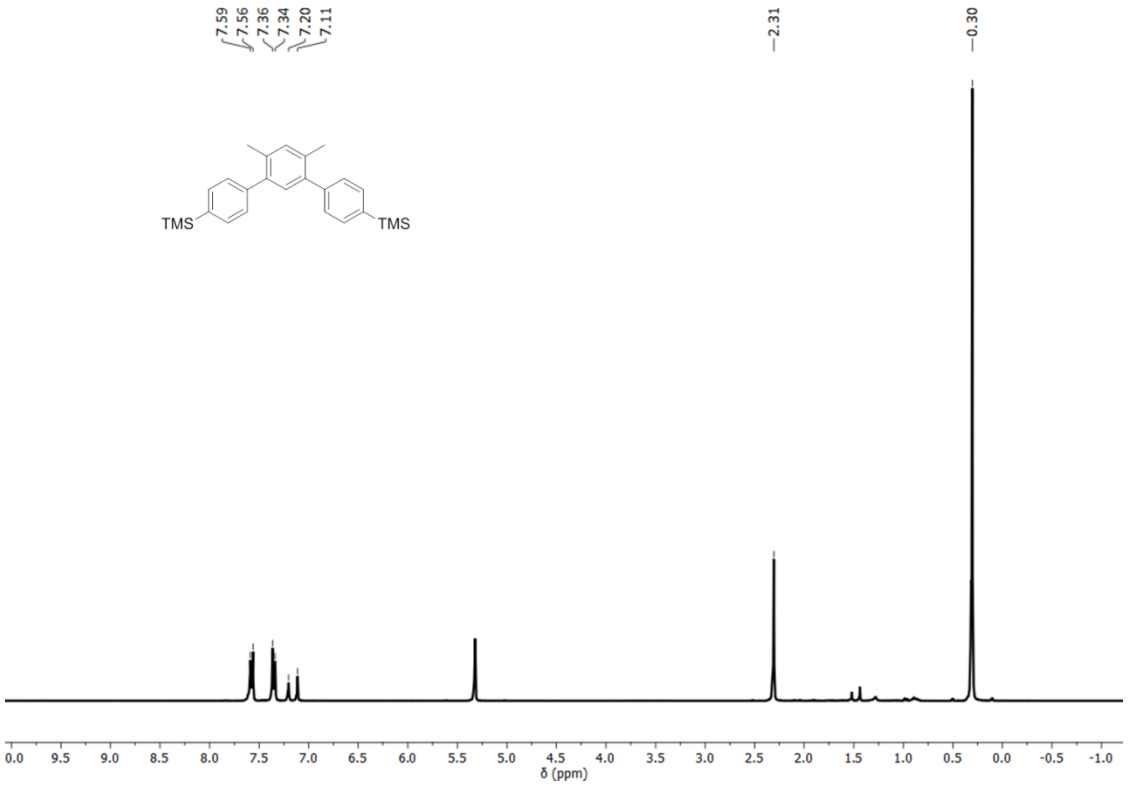

Figure S14. ^{1}H NMR spectrum of 4,4''-bis(trimethylsily)-4',6'-dimethyl-1,1':3',1''-terphenyl (S3) (300 MHz, CD_2Cl_2, 298K).

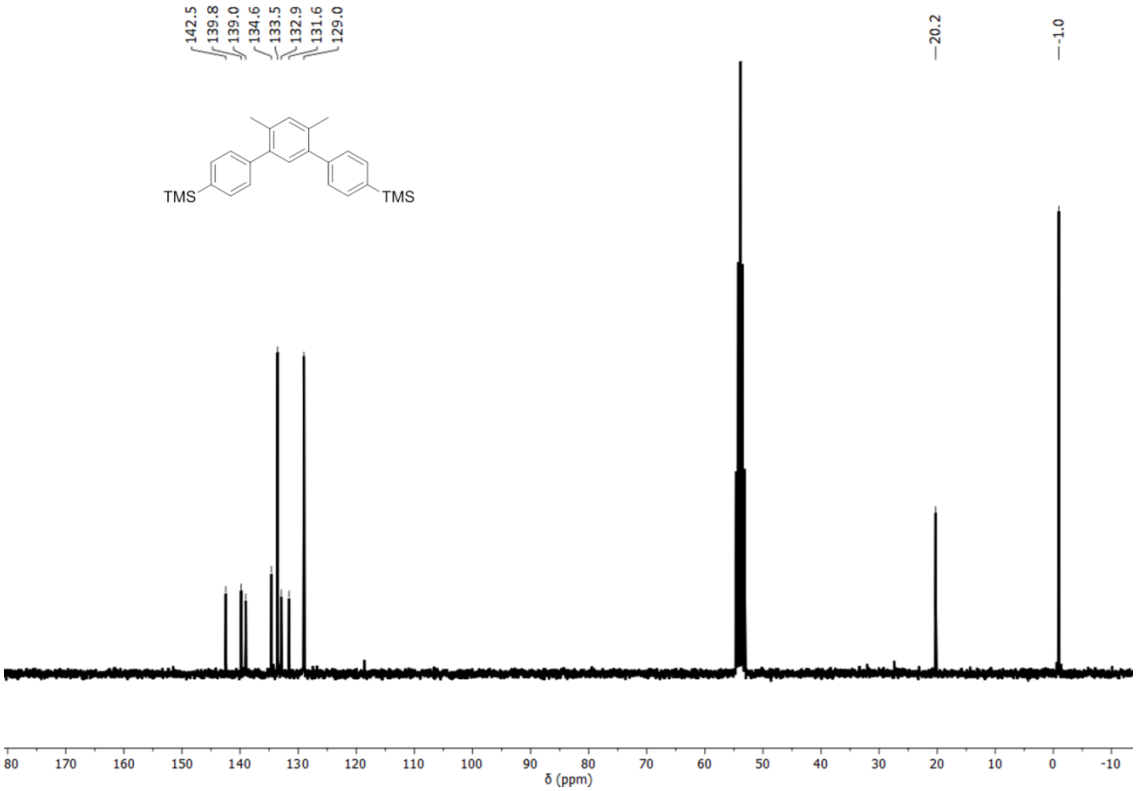

Figure S15. ^{13}C NMR spectrum of 4,4''-bis(trimethylsily)-4',6'-dimethyl-1,1':3',1''-terphenyl (S3) (300 MHz, CD_2Cl_2, 298K).

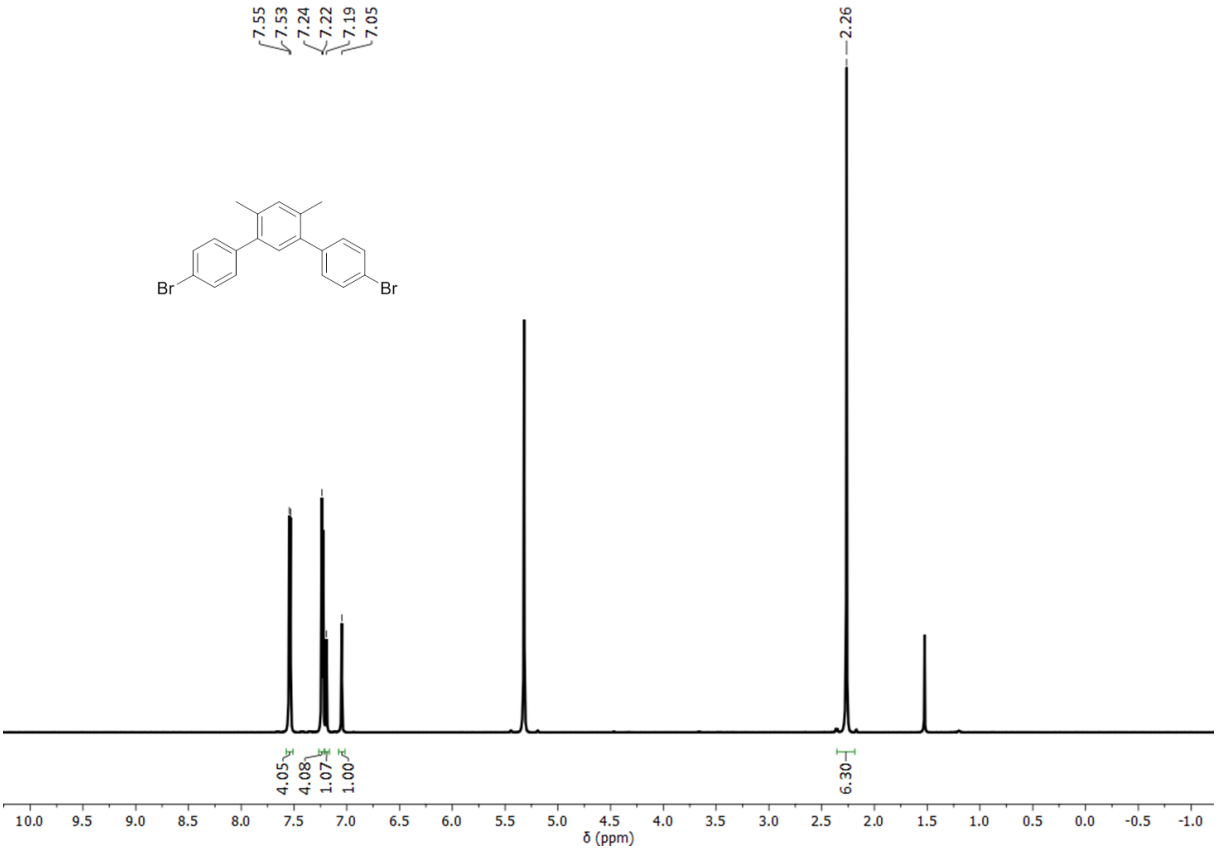

Figure S16. ^{1}H NMR spectrum of 4,4''-dibromo-4',6'-dimethyl-1,1':3',1''-terphenyl (1) (700 MHz, CD_2Cl_2, 298K).

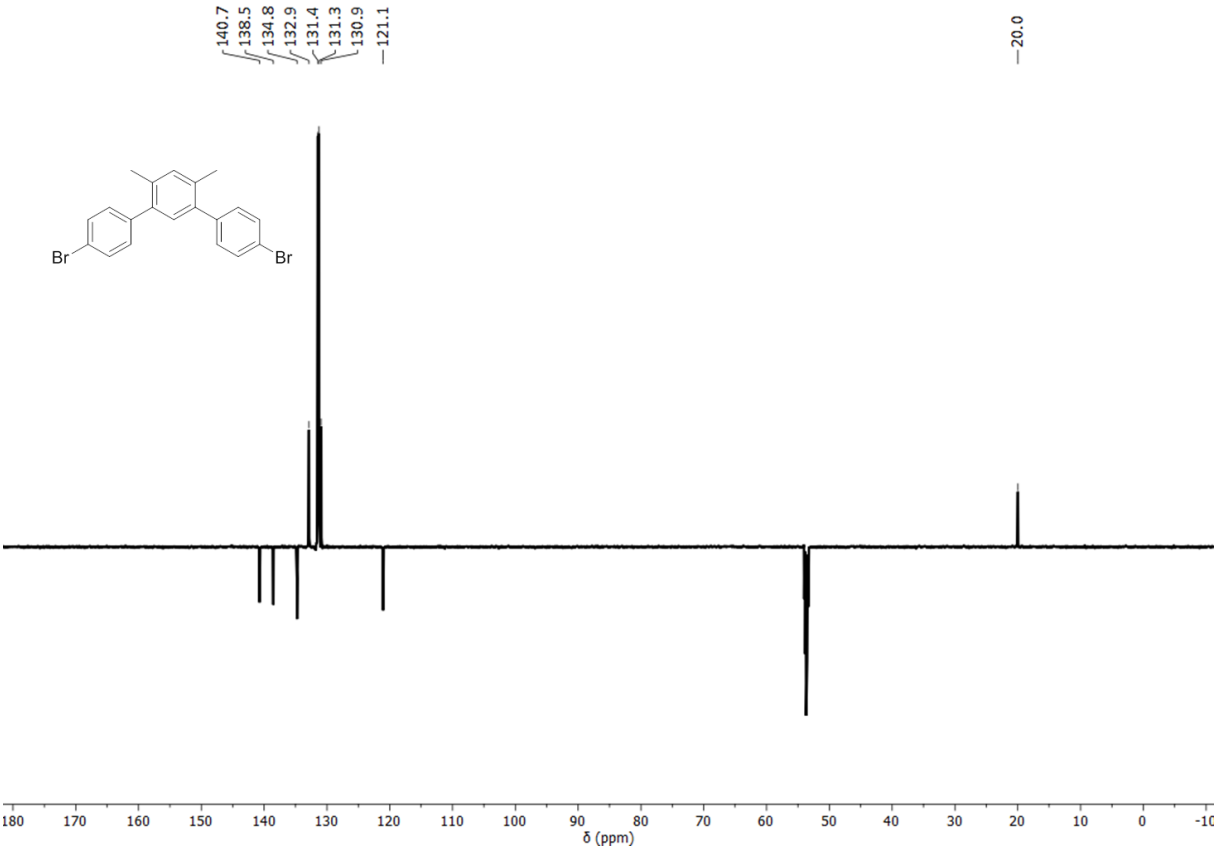

Figure S17. ^{13}C NMR spectrum of 4,4''-dibromo-4',6'-dimethyl-1,1':3',1''-terphenyl (1) (176 MHz, CD_2Cl_2, 298K).

References

(1) Hutter, J.; Iannuzzi, M.; Schiffmann, F.; Vandevondele, J. Cp2k: Atomistic Simulations of Condensed Matter Systems. *Wiley Interdiscip. Rev. Comput. Mol. Sci.* **2014**, *4* (1), 15–25.

(2) Goedecker, S.; Teter, M.; Hutter, J. Separable Dual-Space Gaussian Pseudopotentials. *Phys. Rev. B* **1996**, *54* (3), 1703–1710.

(3) Perdew, J. P.; Burke, K.; Ernzerhof, M. Generalized Gradient Approximation Made Simple. *Phys. Rev. Lett.* **1996**, *77* (18), 3865–3868.

(4) Grimme, S.; Antony, J.; Ehrlich, S.; Krieg, H. A Consistent and Accurate Ab Initio Parametrization of Density Functional Dispersion Correction (DFT-D) for the 94 Elements H-Pu. *J. Chem. Phys.* **2010**, *132* (15), 154104.

(5) Tersoff, J. D.; Hamann, D. R. Theory of the Scanning Tunneling Microscope. *Phys. Rev. B* **1985**, *31* (2), 805–813.

(6) Tersoff, J. D. Method for the Calculation of Scanning Tunneling Microscope Images and Spectra. *Phys. Rev. B* **1989**, *40* (17), 11990–11993.

(7) Hapala, P.; Kichin, G.; Wagner, C.; Tautz, F. S.; Temirov, R.; Jelínek, P. Mechanism of High-Resolution STM/AFM Imaging with Functionalized Tips. *Phys. Rev. B* **2014**, *90* (8), 085421.

(8) Bayly, C. I.; Cieplak, P.; Cornell, W.; Kollman, P. A. A Well-Behaved Electrostatic Potential Based Method Using Charge Restraints for Deriving Atomic Charges: The RESP Model. *J. Phys. Chem.* **1993**, *97* (40), 10269–10280.

(9) Lejaeghere, K.; Bihlmayer, G.; Björkman, T.; Blaha, P.; Blügel, S.; Blum, V.; Caliste, D.; Castelli, I. E.; Clark, S. J.; Corso, A. D.; Gironcoli, S. de; Deutsch, T.; Dewhurst, J. K.; Marco, I. D.; Draxl, C.; Dułak, M.; Eriksson, O.; Flores-Livas, J. A.; Garrity, K. F.; Genovese, L.; Giannozzi, P.; Giantomassi, M.; Goedecker, S.; Gonze, X.; Grånäs, O.; Gross, E. K. U.; Gulans, A.; Gygi, F.; Hamann, D. R.; Hasnip, P. J.; Holzwarth, N. a. W.; Iuşan, D.; Jochym, D. B.; Jollet, F.; Jones, D.; Kresse, G.; Koepernik, K.; Küçükbenli, E.; Kvashnin, Y. O.; Locht, I. L. M.; Lubeck, S.; Marsman, M.; Marzari, N.; Nitzsche, U.; Nordström, L.; Ozaki, T.; Paulatto, L.; Pickard, C. J.; Poelmans, W.; Probert, M. I. J.; Refson, K.; Richter, M.; Rignanese, G.-M.; Saha, S.; Scheffler, M.; Schlipf, M.; Schwarz, K.; Sharma, S.; Tavazza, F.; Thunström, P.; Tkatchenko, A.; Torrent, M.; Vanderbilt, D.; Setten, M. J. van; Speybroeck, V. V.; Wills, J. M.; Yates, J. R.; Zhang, G.-X.; Cottenier, S. Reproducibility in Density Functional Theory Calculations of Solids. *Science* **2016**, *351* (6280), aad3000.

(10) Frisch, M. J.; Trucks, G. W.; Schlegel, H. B.; Scuseria, G. E.; Robb, M. A.; Cheeseman, J. R.; Scalmani, G.; Barone, V.; Mennucci, B.; Petersson, G. A.; Nakatsuji, H.; Caricato, M.; Li, X.; Hratchian, H. P.; Izmaylov, A. F.; Bloino, J.; Zheng, G.; Sonnenberg, J. L.; Hada, M.; Ehara, M.; Toyota, K.; Fukuda, R.; Hasegawa, J.; Ishida, M.; Nakajima, T.; Honda, Y.; Kitao, O.; Nakai, H.; Vreven, T.; Montgomery Jr., J. A.; Peralta, J. E.; Ogliaro, F.; Bearpark, M. J.; Heyd, J.; Brothers, E. N.; Kudin, K. N.; Staroverov, V. N.; Kobayashi, R.; Normand, J.; Raghavachari, K.; Rendell, A. P.; Burant, J. C.; Iyengar, S. S.; Tomasi, J.; Cossi, M.; Rega, N.; Millam, N. J.; Klene, M.; Knox, J. E.; Cross, J. B.; Bakken, V.; Adamo, C.; Jaramillo, J.; Gomperts, R.; Stratmann, R. E.; Yazyev, O.; Austin, A. J.; Cammi, R.; Pomelli, C.; Ochterski, J. W.; Martin, R. L.; Morokuma, K.; Zakrzewski, V. G.; Voth, G. A.; Salvador, P.; Dannenberg, J. J.; Dapprich, S.; Daniels, A. D.; Farkas, Ã.; Foresman, J. B.; Ortiz, J. V.; Cioslowski, J.; Fox, D. J. *Gaussian 09*; Gaussian, Inc.: Wallingford, CT, USA, 2009.

(11) Iikura, H.; Tsuneda, T.; Yanai, T.; Hirao, K. A Long-Range Correction Scheme for Generalized-Gradient-Approximation Exchange Functionals. *J. Chem. Phys.* **2001**, *115* (8), 3540–3544.

(12) Gershoni‐Poranne, R.; Stanger, A. The NICS-XY-Scan: Identification of Local and Global Ring Currents in Multi-Ring Systems. *Chem. – Eur. J.* **2014**, *20* (19), 5673–5688.

(13) Ruud, K.; Helgaker, T.; Bak, K. L.; Jo/rgensen, P.; Jensen, H. J. Aa. Hartree–Fock Limit Magnetizabilities from London Orbitals. *J. Chem. Phys.* **1993**, *99* (5), 3847–3859.